MAPSSIC, a Novel CMOS Intracerebral Positrons Probe for Deep Brain Imaging in Awake and Freely Moving Rats: A Monte Carlo Study

L. Ammour, J. Heymes, M. Bautista, S. Fieux, F. Gensolen, M. Kachel, A. Dubois, F. Lefebvre, F. Pain, P. Pangaud, L. Pinot, J. Baudot, P. Gisquet-Verrier, P. Laniece, C. Morel, L. Zimmer, and M.-A. Verdier

***Abstract*—Preclinical behavior neuroimaging gathers simultaneous assessment of behavior and functional brain imaging. It is a potential key breakthrough to improve the understanding of brain processes and assess the validity of preclinical studies in drug development. Achieving such a combination is difficult, anesthesia or restraints inherent to conventional nuclear imaging preclude its use for behavior studies. In that context, we have proposed an original strategy using submillimetric probes to directly measures positrons inside the rat brain. This paper gives the results of Monte Carlo simulations of a new generation of intracerebral positron probe based on a complementary metal oxide semi-conductor monolithic active pixel sensor. We present the results obtained for a probe into a large homogeneous volume of radioactive water (^{18}F) leading to a sensitivity of 0.88 cps·Bq^{-1}·mm^3 and a mean energy deposition by positrons of 15.1 keV. Simulation in simplified brain-shaped sources modeling a ^{11}C-raclopride experiment shows that the implanted volume modeling the left putamen contribute to 92.4% of the signal from positrons. We also investigate the effects of the thickness of the sensitive layer, the energy threshold and pixel dimensions on the detection capacities of the sensor. We demonstrate that an increase in the sensitive thickness from 18 to 190 μm would lead to an increase of positrons sensitivity by a factor of 1.74, but to a decrease of the direct (positrons) to indirect (γ-rays and electrons) sensitivity ratio by a factor of 1.59. Finally, we show that for a threshold lower than about 5 keV the effect of the pixel dimensions is negligible.**

Manuscript received February 21, 2018; revised June 15, 2018 and October 1, 2018; accepted October 6, 2018. Date of publication November 14, 2018; date of current version May 2, 2019. This work was supported in part by the Project *Instrumentation aux limites* from CNRS in 2015 and 2017, in part by the France Life Imaging of the French Investissements d'Avenir program run by the Agence Nationale pour la Recherche under Grant FLI/ANR-11-INBS-0006, and in part by IN2P3. *(Corresponding author: M.-A. Verdier.)*

L. Ammour, A. Dubois, F. Lefebvre, F. Pain, L. Pinot, and P. Laniece are with the Department of Physics, University of Paris-Sud, 91405 Orsay, France, and also with the Laboratory of Imaging and Modeling in Neurobiology and Oncology, CNRS-IN2P3, University of Paris-Diderot, 91405 Orsay, France.

J. Heymes, M. Kachel, and J. Baudot are with CNRS, IPHC UMR 7178, Université de Strasbourg, 67000 Strasbourg, France.

M. Bautista, F. Gensolen, P. Pangaud, and C. Morel are with CNRS/IN2P3, Aix-Marseille University, 13288 Marseille, France.

S. Fieux and L. Zimmer are with Lyon Neuroscience Research Center, CNRS/INSERM, University of Lyon 1, 69100 Lyon, France.

P. Gisquet-Verrier is with CNRS, UMR 9197, University of Paris-Sud, Neuroscience Paris-Saclay Institute, 91405 Orsay, France.

M.-A. Verdier is with the Laboratory Imaging and Modeling in Neurobiology and Oncology, CNRS-IN2P3, University of Paris-Diderot, Sorbonne Paris Cité, 91405 Orsay, France (e-mail: verdier@imnc.in2p3.fr).

Color versions of one or more of the figures in this paper are available online at http://ieeexplore.ieee.org.

Digital Object Identifier 10.1109/TRPMS.2018.2881301

***Index Terms*—Active pixel sensors, Animal behavior, CMOS Image sensors, Implants, Molecular imaging, Monte Carlo methods, Nuclear Imaging, Positron emission tomography.**

I. Introduction

AMONG the numerous methods developed to address neuroscience research needs, the combination of positron emission tomography (PET) with behavioral studies has been pointed out as a potential key breakthrough to go further in the understanding of functional processes in the brain [1]. Correlating *in vivo* molecular processes of neuronal communication with behavior in real time is of major interest. This complementarity is a critical step for comparing animal to human behavior and consequently assess the validity of preclinical studies in drug development. For example, as explained in [2], behavior neuroimaging shows applications for the study of addiction in animal models, using ^{18}F-FDG for associating brain metabolism to a particular behavior or ^{11}C-raclopride to study the dynamic changes in the dopaminergic system in real-time.

Achieving such a combination is not straight-forward though, since general anesthesia or severe restraints historically used in small animal PET imaging precludes its use for behavioral studies.

Furthermore, previous works have highlighted that anesthesia or restraints on awake animals affect PET brain imaging studies ability to reflect the awake and freely moving rat brain [3], [4]. As pointed out by Alstrup and Smith, anesthesia effects does not preclude PET brain imaging, but the current procedures to evaluate its effects using PET show limitations. For instance, awake imaging with restraints may cause stress to the animals. This points out the relevance for new tools for radiotracers imaging on awake animals and without restraints.

To address these obstacles, several approaches have been studied but remain affected by important constraints. The simplest method, the sequential use of anesthetized PET imaging after behavior experiment (as described in [2]) is obviously counterbalanced by the lack of real time analysis. A second method, the tracking of the rodent position inside a PET gantry [5] restricts the rat movements within its field of view, thus limiting the ability to perform complex behavioral studies. The RatCAP, which relies on a wearable PET for imaging

the entire brain on awake animals, still requires a mechanical arm to sustain the device [6].

In that context, a less cumbersome strategy was proposed to record the radiotracers time-activity curves: radiosensitive positron probes. Directly at the contact of rodent tissue, they allow to measure the radioactivity in the region of interest, i.e., the medium surrounding the sensor, while leaving the animal freely moving. Without providing a full brain image, they are a simple and cost effective tool with a good sensitivity. Hence, they are an effective way to assess local time activity curves.

The first probes used a scintillation detector coupled to an external photomultiplier tube [7], [8], then extended to fully autonomous systems thanks to reverse-biased, high-resistivity silicon diodes, and wireless communication [9].

These probes, implanted by stereotaxic surgery or placed closed to the brain surface must have a reduced size compatible with those of studied brain structures and must be biocompatible. Their sensor has to be highly sensitive to β^+ particles and has to present a good transparency to annihilation γ-rays.

A first intracerebral wireless probe named PIXSIC was previously developed [10]. Although successfully validated in various biological contexts [11], providing promising results for behavioral neuroimaging, this probe design suffered from several issues. The probe sensitivity to γ-rays led on to substantial noise. Moreover, the thickness of the probe, reduced to 200 μm to limit annihilation γ-rays interactions, made the device brittle and difficult to manipulate. Finally, the signal suffered from electromagnetic noise picked-up along the tracks, as the charge had to be transported on a distance of about two centimeters.

Taking into account these limits we considered complementary metal oxide semi-conductor (CMOS) monolithic active pixel sensor (MAPS) technology to develop a novel β^+ sensitive micro-probe called MAPSSIC. In particular, among other benefits, MAPS provides direct signal amplification at pixel level, leading to a high signal to noise ratio. Moreover, the thickness of the epitaxial sensitive layer, a few tens of micrometers thick, should provide a good transparency to 511 keV γ-rays.

In order to find the most suitable sensor for the probe, we conducted Monte Carlo simulations to optimize the sensor developments. We simulated a sensor based on first design guidelines, which will be described in Section II-A, as biological, electronics and mechanical constraints. This model was placed at the center of a homogeneous aqueous solution of ^{18}F, ^{15}O, or ^{11}C or into a simplified sources model of an ^{11}C-raclopride experiment. The simulations evaluated the physical detection properties, without accounting for signal processing nor charges diffusion.

II. Methods

A. Sensor Model

We have designed a first set of CMOS probes matching miniaturization requirements for brain implantation and technical feasibility of CMOS MAPS sensors.

To be inserted into the brain of a rat, the sensor is needle shaped. Its width should not be greater than approximately 500 μm in order to limit the invasiveness in cerebral tissues while providing a large sensitive volume. Its length must exceed 1 cm in order to attach the implanted sensor to a head socket, which is set on the rodent skull. The MAPS sensor circuit was designed to be manufactured in a 180 nm CMOS image sensor technology, with a high resistivity epitaxial layer sensitive to charged particles. This epitaxial layer can be grown to a thickness ranging from 18 to 40 μm with pixel dimensions in the order of a few tens of micrometers. Moreover, polarization of the substrate to reach deep depletion is possible in this type of CMOS technology allowing a thicker sensitive region, up to the whole silicon thickness [12].

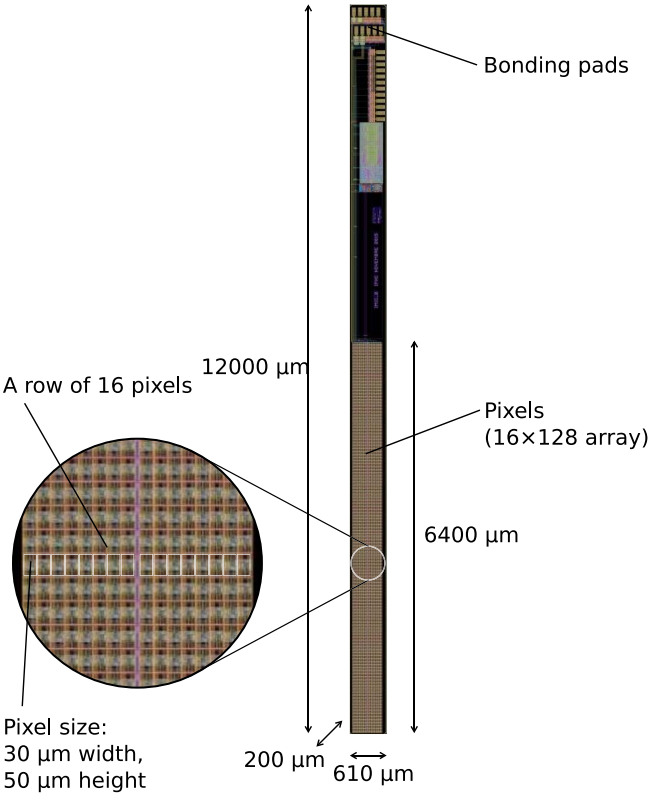

Fig. 1. Model of the first sensor prototype. It features a 16 × 128 pixels matrix for charged particles detection, each pixel surface is 30 × 50 μm^2. The pixels are made into a thin 18 μm epitaxial layer. The whole sensor dimensions are 12 mm length, 610 μm width, and 200 μm thick.

A first prototype of the sensor called IMIC was designed as a 12 mm long silicon parallelepiped, with a 610 μm width and a thickness of 200 μm. The sensor architecture is based on the ALPIDE chip developed for the ALICE experiment at the CERN Large Hadron Collider [13]. The first 10 μm in depth receive the CMOS process, then comes the epitaxial layer over a 18 μm thickness. The pixel matrix features 16 columns and 128 rows. The pixel dimensions are 50 μm along the probe length (longest dimension) and 30 μm along its width. The matrix of pixels is set on the lower half of the probe. The layout of the sensor model is presented in Fig. 1.

B. Detection Properties

The first aim of this paper was to validate the sensor concept, by demonstrating its ability to quantify the concentration

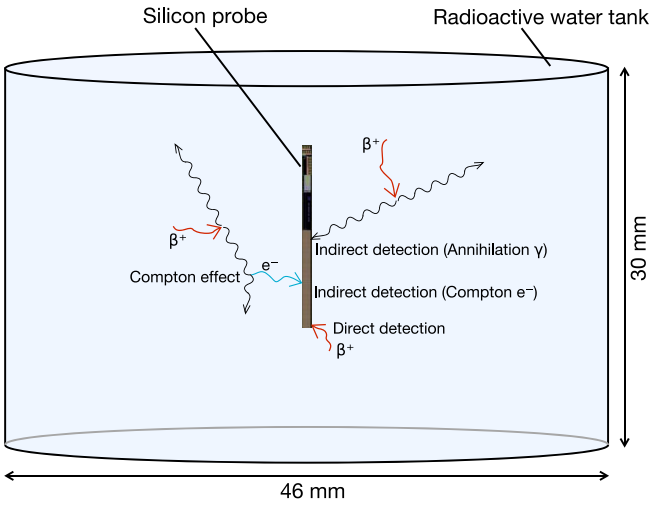

Fig. 2. MAPSSIC sensor model into a cylindrical source of β^+ radioactive water. Three types of signal source in the sensor are illustrated here. From top to bottom: the detection of an annihilation γ-ray, the detection of an e^- consecutive to a Compton effect in the surrounding medium and the direct detection of a β^+ emitted by the source close to the pixels. The contribution to the signal from the first two types of events is called "indirect."

of radioactivity in experimental context and exhibit improved performances, as compared to previous probes.

To evaluate the sensor design, we first studied several detection properties: detection efficiency, deposited energy, and sensitivity of the sensor.

The second goal was to optimize the design and the parameters of the probe, on the basis of these properties. We aimed to optimize the epitaxial layer thickness and pixel dimensions by using Monte Carlo simulations in order to create a set of parameter models.

1) Direct and Indirect Detection: In order to evaluate the detection properties, we distinguished the direct and indirect detection of positrons. When an event is created by a positron emitted by the source, directly interacting in the sensor, it gives information about the radioactive concentration in the vicinity of the probe because of the short positron range in water or brain tissues. This corresponds to direct positron events. On the other hand, annihilation γ-rays and Compton electrons (issued from annihilation rays interacting within the surrounding medium) can also create events in the sensor, but their corresponding source emission location cannot be restricted to the close environment of the probe because of the high penetration of 511 keV annihilation γ-rays. They are consequently indirect positron events. Fig. 2 illustrates these different signal components.

2) Detection Efficiency: For a given small volume v at the position in a source volume, the detection efficiency e is defined as the ratio between the rate of counted events originating from v, N (cps), and the activity in this volume A (Bq)

$$e = \frac{N}{A}. \tag{1}$$

3) Sensitivity: The sensitivity is defined as the counts rate of events N_{source} (cps) per unit of radioactivity concentration C_{ref} (Bq·mm^{-3}) of a reference source

$$S(\text{cps}\cdot\text{Bq}^{-1}\cdot\text{mm}^3) = \frac{N_{\text{source}}}{C_{\text{ref}}}. \tag{2}$$

If a source volume is discretized into small elements (voxels) i with volumes v_i, activity concentrations C_i and efficiencies e_i, the sensitivity to this source volume is expressed by:

$$S = \frac{1}{C_{\text{ref}}} \sum_i e_i \times C_i \times v_i. \tag{3}$$

We also define the direct sensitivity as the sensitivity to direct positron events and the indirect sensitivity when counts are related to indirect detection events. As the direct sensitivity always provides useful information about radioactivity concentration in the surrounding medium whereas the indirect sensitivity could lead to signal originating from remote sources, the ratio between direct sensitivity, and indirect sensitivity is considered as a metric of signal to noise ratio [7], [14].

4) Deposited Energy: The deposited energy is measured in the sensitive part of the sensor. For a given event, it is the sum of the deposited energy by an incident particle and all the secondary particles created in the sensitive volume.

5) Optimization of Sensitive Thickness and the Pixel Dimensions: Considering the various sensitive layer thicknesses allowed by the CMOS technology ranging from 18 μm, up to the entire thickness except the wiring layer, we aimed to evaluate the effects of these sensitive thicknesses on detection properties. Moreover, the dimension of the pixels can also be adjusted. The first prototype used 30×50 μm^2 pixels. MAPS sensor would allow smaller pixels (20×20 μm^2 with MIMOSA32 sensors [15] built with the same CMOS process).

C. Design of the Simulation

1) Sensor Geometry: Monte Carlo simulations were performed using GATE 7.0 [16], [17]. The probe model was defined according to the first design previously presented: a first $610 \times 200 \times 12000$ μm^3 parallelepiped of silicon, simulating the sensor, encapsulating an inner silicon $480 \times 190 \times 6400$ μm^3 parallelepiped, simulating the sensitive volume of the sensor (see Fig. 3). This latter parallelepiped was defined in the simulation as a sensitive volume, within which all the interactions of particles are stored. This volume is larger than the 18 μm thick epitaxial region to allow the study of models with a larger sensitive thickness.

2) Source and Phantom: The simulated source was an aqueous homogeneous solution of either ^{18}F or ^{11}C or ^{15}O, radioactive β^+ emitters with energies of 633.9, 960.5, and 1735.0 keV, respectively. The source fills out a cylindrical volume of 30 mm height, and 46 mm diameter, as illustrated in Fig. 2. The simulated probes were located at the center of the source.

3) Physical Processes: The physics processes were simulated using the *Penelope* model (the Geant4 implementation of the physics models developed for the PENELOPE code, including reliable electromagnetic processes for photons, electrons, and positrons at low energies [16]). All energy cuts (minimum energy threshold of secondary particles production)

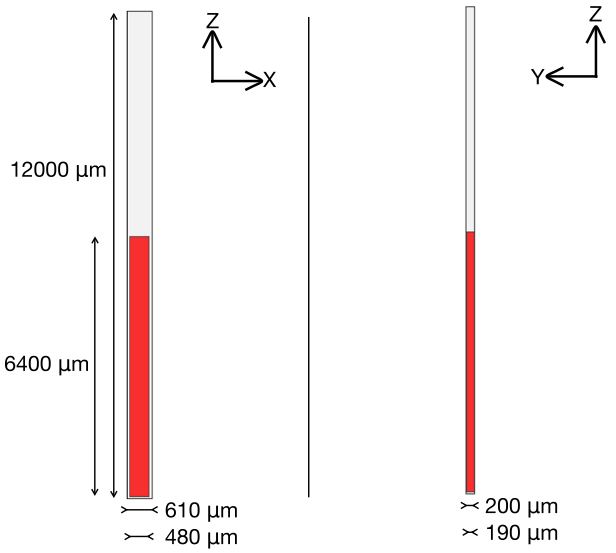

Fig. 3. GATE sensor model, made of two silicon parallelepipeds. The outer parallelepiped dimensions are $610 \times 200 \times 12000$ μm^3. The inner red parallelepiped dimensions are $480 \times 190 \times 6400$ μm^3. We recorded all the events occurring in the sensitive volume (in red). Pixels are not modeled in this GATE simulation but during data analysis with the required shapes and sizes. The left figure is a cross section in the (*Z, Y*) plan, the right figure is a cross section in the (*Z, X*) plan.

were set to the energy corresponding to a 1 μm interaction path length in the medium.

We recorded all physical interactions, called *hits*, occurring in the sensitive inner volume: their type, particles involved, their location, the amount of deposited energy, a unique identification number of the source emission leading to this event and the location of this emission. When several recorded hits have the same primary particle for origin, this group of hits is called *event*.

D. Numerical Analysis

1) Sensitive Thickness: To fit the simulation model to the sensor design, we had to filter the recorded data. As we simulated a 190 μm thick sensitive area we filtered all recorded interactions occurring below a thickness of 18 μm, corresponding to the epitaxial thickness of our first prototype, or thicker in order to study the effects of the sensitive thickness variation on the detection parameters.

2) Pixels Boundaries: Although we did not model the individual pixel boundaries with GATE, all the positions of interaction were recorded. Consequently we were able to sort the recorded hits pixels by pixels during post-analysis. This allowed us to change the dimensions and number of the pixels to study their impact on the detection performances.

3) Energy Thresholds: We have defined detection energy thresholds the following way: events were kept if the sum of deposited energy in at least one pixel was above a given value. While evaluating the detection properties we studied the impact of energy thresholds on detection properties, from no energy threshold up to a 40 keV threshold.

4) Voxelized Phantom: Finally, by keeping or rejecting events based on the position of their primary particle emission, we were able to modify the spatial distribution of the source. We used a voxelized source file containing voxels activities as input. Each group of recorded events related to the same source emission were randomly kept with a probability equals to the relative voxel activity where this emission was located.

TABLE I
DIMENSIONS AND ACTIVITY CONCENTRATIONS OF THE SIMPLIFIED BRAIN MODEL VOLUMES

Structure	Relative activity concentration	Dimensions (X, Y, Z) (mm)
R.O.B.	0.16	(20, 14, 10)
Cerebellum	0.11	(7, 10, 7)
L. CPu.	0.64	(3.5, 3.5, 5.5)
R. CPu.	0.64	(3.5, 3.5, 5.5)
L. HG.	1.0	(5, 10, 7)
R. HG.	1.0	(5, 10, 7)

In order to model a realistic source distribution, we defined a simple voxelized brain phantom model of a rat brain (see Fig. 4). It is made of six parallelepiped volumes: left and right harderian glands (L. HG. and R. HG.), left and right caudate putamen (L. CPu. and R. CPu.), cerebellum and rest of the brain (R.O.B.). Dimensions were based on the Paxinos and Watson rat brain atlas [18].

In order to model ^{11}C-raclopride experiments, the phantom was based on the simulated ^{11}C source. The activity values were based on the reference time activity curve published in the OSSI-PET database [19].

The sensor was placed vertically at the center of the simplified left caudate putamen region. As this region height is smaller than the sensitive volume height, a section of 5.5 mm height of the sensitive volume was into the L. CPu. and a section of 0.9 mm was into the R.O.B. Fig. 4 illustrates two cross sections of this phantom. The corresponding dimensions and activities are presented in Table I.

5) Efficiency Spatial Distribution: Based on the simulations of the whole cylindrical source, with a 18 μm thick sensitive area and assuming no energy threshold, we have evaluated the detection efficiency within the source volume. The source positions of the recorded events were discretized into small volume elements (voxels). We computed each voxel efficiency as the ratio between the rate of detected events originating from a given voxel and the total activity in the voxel volume defined in our simulation model. Our sources models only generated β^+ (branching ratio is 1).

We also computed the volume where efficiency exceed some values (10 %, 1 %, and 0.1 %).

6) Deposited Energy: The deposited energy was evaluated for the whole cylindrical sources, and for the three isotopes of interest. We compared the spectra of the deposited energy for each incident particles type. The incident and secondary particles can interact in different pixels, thus their energy can be deposited in several pixels. Since only one pixel hit is needed for an event to be detected, we studied only the pixel were the total deposited energy was the highest.

7) Sensitivity: The sensitivity was computed using (2). The activity concentration was defined in the GATE

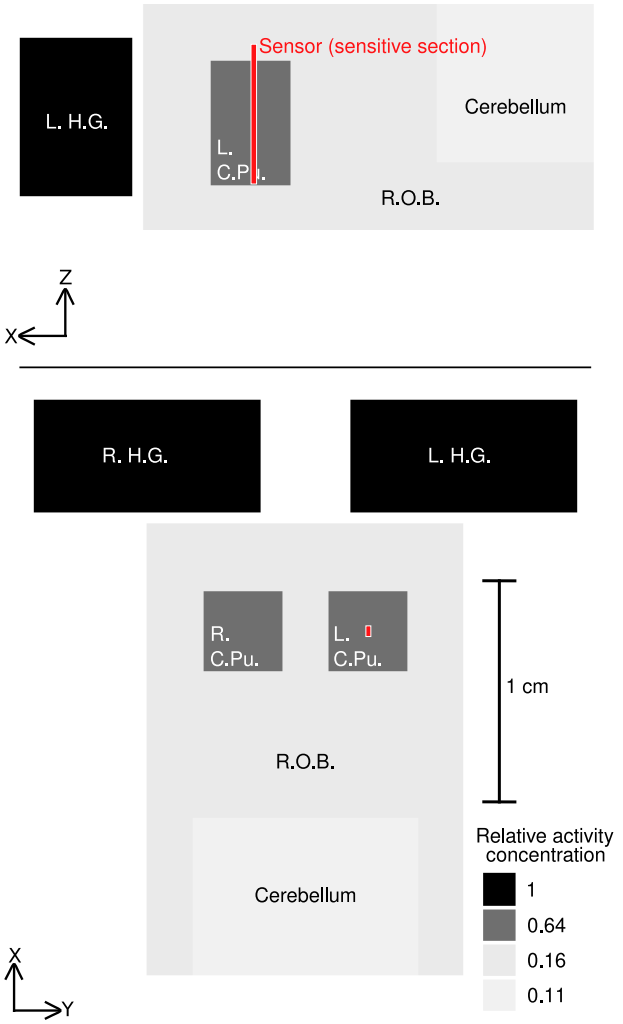

Fig. 4. Simplified simulated model of the rat brain including six volumes: left and right harderian glands (L. HG. and R. HG.), left and right caudate putamen (L. CPu. and R. CPu.), cerebellum and rest of the brain (R.O.B.). The sensor properties are computed within this model. The probe (in red) is implanted in the middle of the L. CPu. structure. The activity concentration distribution follows a realistic ^{11}C-raclopride experiment, the gray level is proportional to the activity. The top cross section presents the model of the (*Z, X*) plan, the bottom figure is a cross section of the (*X, Y*) plan. Both cross sections use the same activity concentration and dimension scales.

model, 1.60×10^6 Bq·mm^{-3} for the cylindrical ^{18}F source, 0.80×10^6 Bq·mm^{-3} for the cylindrical ^{15}O source, and 1.59×10^6 Bq·mm^{-3} for the ^{11}C cylindrical and brain phantom sources.

Direct and indirect sensitivities and their ratios were first evaluated for the homogeneous radioactive cylindrical sources. By adapting the spatial distribution of the source into a set of homogeneous cylindrical sources with different radii, we obtained sensitivity values as a function of the source radius.

We compared the results of the largest cylinder source with the previous PIXSIC probe. As the previous sensor geometry was different from the simulated one, we compared the sensitivity from equivalent heights h_{eq}. The equivalent sensitivity S_{eq} was computed as the mean sensitivity in a section of height h_{eq}, i.e., the sensitivity within the entire sensor multiplied by the ratio of the equivalent height to the sensor total height. The equivalent height was $h_{eq} = 500$ μm, as presented in [10].

We have also compared the sensitivity of each MAPSSIC sensor pixel for an array of 128×16 pixels. As for deposited energy computation, we took into account the events only in the pixel of maximum deposited energy. We have compared the mean sensitivity of edge pixels and center pixel. We have evaluated the nonuniformity of the sensor using the integral uniformity (IU) metric, defined as

$$\mathrm{IU} = \frac{S_{\max} - S_{\min}}{S_{\max} + S_{\min}} \tag{4}$$

where $S_{\min}$ is the minimum pixel sensitivity value and $S_{\max}$ is the maximum pixel sensitivity value, after removing the edge pixels and applying a nine points filter as described in [20].

Finally, we computed the sensitivities in the brain shaped voxelized phantom, with the sensor placed at the center of the L. CPu. region.

III. Results

A. Efficiency

The spatial detection efficiency of the entire probe into a phantom filled with ^{18}F solution is shown in Fig. 5. Fig. 5(a) presents the direct detection efficiency of the sensor while Fig. 5(b) shows the indirect detection efficiency. Efficiency isolines at 10 % and 1 % levels are drawn.

Each figure presents two slices of the detection efficiency, one along the sensor length (made of $0.1 \times 0.1 \times 5.5$ mm pixels) and the other one perpendicularly to it (made of $0.1 \times 0.1 \times 0.6$ mm pixels).

As expected, the low range of positrons in water strictly restricts the region of direct detection to a small region around the sensor. Moreover, the direct detection efficiency quickly decreases with the radius, demonstrating that the major contribution to the signal originates from the sensor vicinity. For ^{18}F, the efficiency drops to less than 1 % at 1.06 mm from sensor surface. Both the direct and the indirect efficiencies decrease with distance to the sensor due to the lower detection solid angle.

As the sensitive volume thickness is 18 μm and located between two very asymmetrical layers of silicon, of 10 μm on one side and 152 μm on the other side, this leads to a strong asymmetry on the efficiency along the *y*-axis.

The volume bounded by the 1 % efficiency isosurface (for direct events, in a ^{18}F water phantom) is as small as 17.34 mm^3. Other isoefficiency volumes are presented in Table II. As a matter of comparison, volumes of typical studied rat brain structures, hippocampus, or caudate putamen, are, respectively, 39.5 and 31.0 mm^3 according to [21] and [22]. Consequently we can expect a good detection efficiency of the radioactivity in the region of interest while limiting the efficiency to sources outside of this region.

B. Sensitivity

The sensitivity varies greatly as a function of the source radius as shown on Fig. 6. Under radii close to the positron

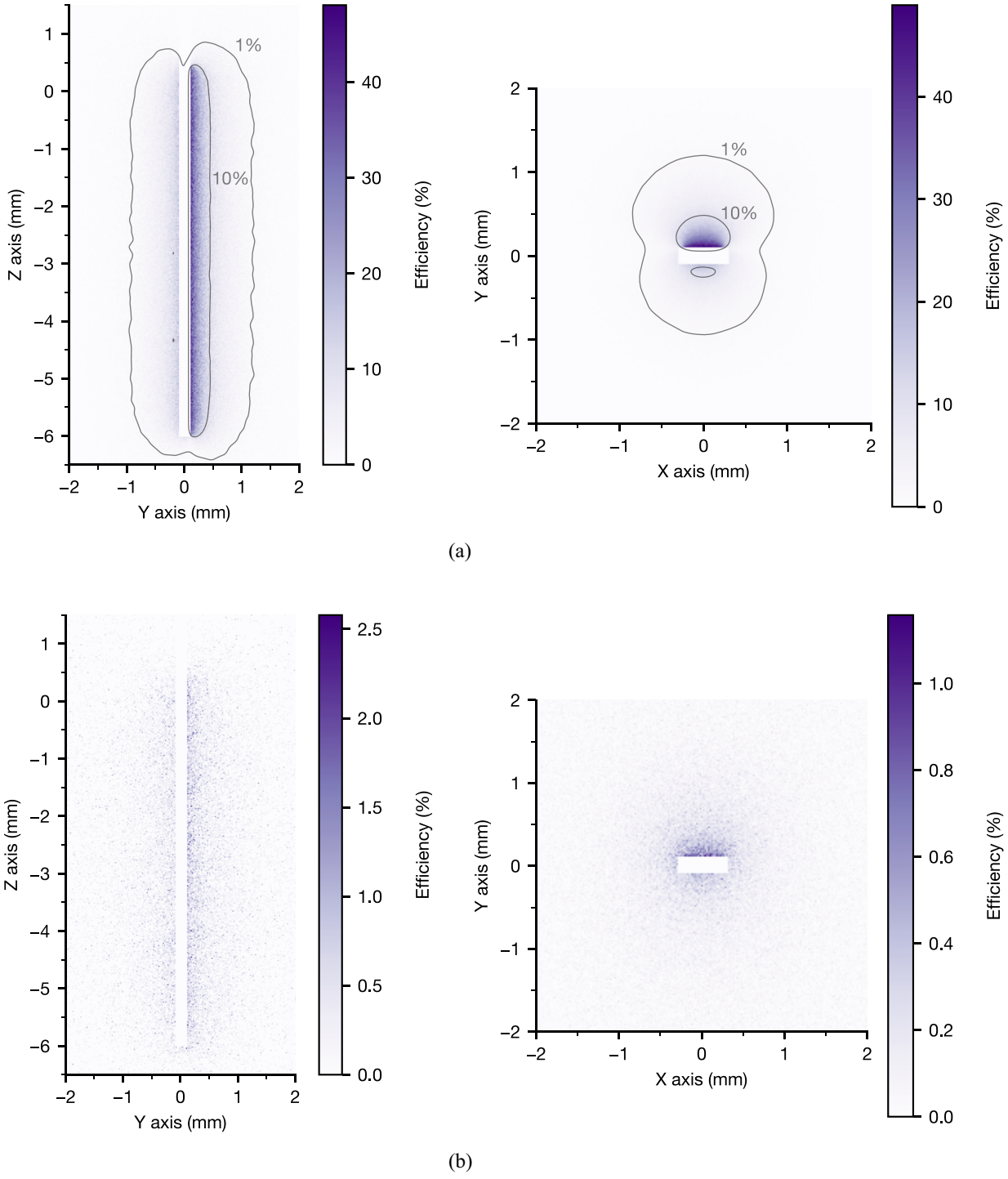

Fig. 5. Spatial distribution of the direct (top) and indirect (bottom) detection efficiency of the sensor into an homogeneous radioactive ^{18}F solution in water. The left figures present a lateral cross section, including the complete sensitive region [(*Z, Y*) plan], the right ones present cross sections perpendicular to the sensor axis [(*X, Y*) plan]. The sensor shape is displayed at the center of the figures, as a null efficiency area. The 10 % and 1 % efficiency isolines are drawn, smoothed to improve readability. (a) Direct efficiency map. (b) Indirect efficiency map.

range in water (2.3 mm for ^{18}F according to [23]), the sensitivity to direct events quickly increases with the diameter of the source. For larger radii, the direct sensitivity stops increasing, as efficiency for the furthest points drops to zero.

For ^{18}F, this direct sensitivity limit was computed at (8.83 $\pm$ 0.01) $\times$ 10^{-1} cps·Bq^{-1}·mm^3. The maximum is obtained for a 2.71 mm cylinder radius, it reaches 99.9 % of this value for a 2.12 mm radius. The direct sensitivities for the three isotopes are summarized in Table III. We observed a greater direct sensitivity for ^{11}C and ^{15}O sources than for ^{18}F sources. This difference arises from the positrons larger range in water for these isotopes.

Indirect sensitivity continuously increases because of the high penetration of annihilation γ-rays in water. Even if we

TABLE II
VOLUMES BOUNDED BY THE 10 %, 1 %, AND 0.1 % ISOEFFICIENCY SURFACES FOR DIRECT POSITRONS DETECTION FROM THREE RADIOACTIVE SOURCES (^{18}F, ^{11}C, AND ^{15}O) IN WATER

Source	Structure name	Volume (mm^3)
^{18}F	V10%	1.49 ± 0.01
	V1%	17.34 ± 0.05
	V0.1%	54.62 ± 0.08
^{11}C	V10%	2.25 ± 0.02
	V1%	37.52 ± 0.07
	V0.1%	109.05 ± 0.08
^{15}O	V10%	3.12 ± 0.03
	V1%	80.13 ± 0.08
	V0.1%	120.68 ± 0.03

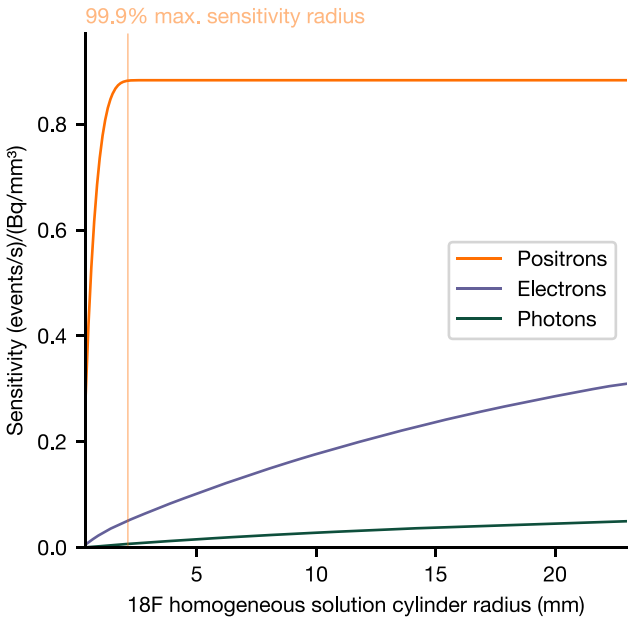

Fig. 6. Sensor sensitivity as a function of the cylindrical phantom radius. The phantom is filled with an homogeneous ^{18}F solution. The vertical line illustrates the radius where sensitivity to positrons reaches 99.9 % of its maximum, at 2.12 mm. Sensitivity is separated into three contribution: direct positron detection (the emitted positron reaches the sensitive area), indirect positron detection where a photon or an electron interact in the sensitive area.

have demonstrated a low detection efficiency to indirect event in the remote medium (due to the solid angle), its integration over increasing cylinder volumes leads to a non negligible contribution to sensitivity for large radii. Table III presents the radius of an homogeneous radioactive cylinder associated with direct to indirect sensitivity ratios of 20, 10, and 5. As for direct sensitivity, higher energy positron sources produce better direct to indirect ratios. These results cannot be directly interpreted as estimates of the direct to indirect sensitivity ratio in biological experiments since the source distribution differs from the homogeneous cylindrical case and does not model remote hot-spots resulting from the bladder or heart. However, we observe that an homogeneous cylinder of 7 mm radius and 30 mm height, which is roughly equivalent to a rat brain and nearby structures able to bind tracers like ^{11}C-raclopride or

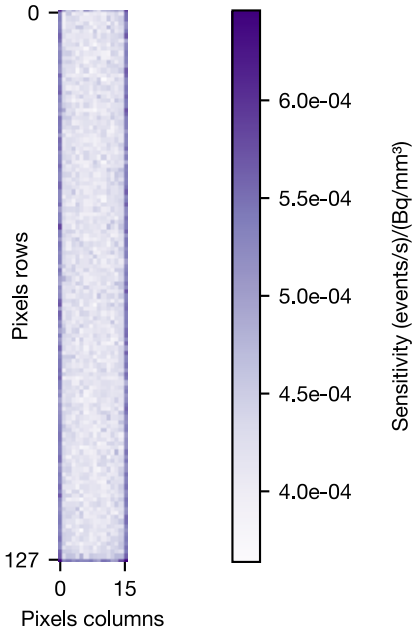

Fig. 7. Sensitivity map over the 16×128 pixels, each one featuring a 30×50 μm^2 area. The sensor was placed at the center of a homogeneous ^{18}F cylindrical source.

^{18}F-FDG, would lead to a 17.77 and 10.50 sensitivity ratio for ^{15}O and ^{11}C sources, respectively, but only 5.71 for ^{18}F. Thus, one should pay particular attention to the signal associated with the entire brain background radioactivity for ^{18}F-based tracers studies.

In order to compare the new sensor sensitivity to the previous PIXSIC one, we computed equivalent sensitivity (mean total sensitivity for a 500 μm height section of the sensor). Into the same large homogeneous water phantom of ^{18}F, the PIXSIC equivalent sensitivity was computed by Monte Carlo simulations to 8.1×10^{-2} cps·Bq^{-1}·mm^3 and was experimentally measured to be equal to $(8.0 \pm 0.6) \times 10^{-2}$ cps·Bq^{-1}·mm^3 for a 500 μm height section. For the new sensor we found a mean value of $(9.72 \pm 0.01) \times 10^{-2}$ cps·Bq^{-1}·mm^3 for 500 μm height.

This comparison was done with different energy thresholds. PIXSIC simulation results were obtained using a 20 keV energy threshold [10] while our simulations did not accounted for any energy threshold. The PIXSIC diodes require an amplification circuit outside of the sensor, leading to high levels of noise, compensated in experimental studies by a high energy threshold. For MAPS pixels, we expect this energy threshold to be low: the ALPIDE pixels experimental studies used a threshold setting inferior to 1 keV [13].

Fig. 7 presents the pixel sensitivity over an array of 16×128 pixels of 30×50 μm^2 each.

The mean sensitivity with one standard deviation in the central area (excluding the first outer edge pixels) is $(4.19 \pm 0.18) \times 10^{-4}$ cps·Bq^{-1}·mm^3. The edge mean sensitivity value is 5.31×10^{-4} cps·Bq^{-1}·mm^3, with a standard deviation equals to 2.55×10^{-5} cps·Bq^{-1}·mm^3. We notice a higher sensitivity on the edge (mean sensitivity increased by 26.8 %), because of geometrical and physical effects. The integral

TABLE III
MAXIMUM DIRECT SENSITIVITY VALUES AND RADII ASSOCIATED WITH A GIVEN LEVEL OF DIRECT SENSITIVITY AND WITH VARIOUS RATIOS OF DIRECT TO INDIRECT SENSITIVITY VALUES, FOR THE ^{18}F, ^{11}C, AND ^{15}O HOMOGENEOUS CYLINDRICAL SOURCES IN WATER

Source	^{18}F	^{11}C	^{15}O
S^{max}_{direct} (cps · Bq^{-1} · mm^3)	$(8.83 \pm 0.01) \times 10^{-1}$	1.79 ± 0.01	4.34 ± 0.01
$50\%S^{max}_{direct}$ radius (mm)	0.50	0.77	1.6
$99\%S^{max}_{direct}$ radius (mm)	1.73	2.85	5.96
$99.9\%S^{max}_{direct}$ radius (mm)	2.12	3.53	7.36
$\frac{S_{direct}}{S_{indirect}} = 20$ radius (mm)	1.53	2.96	5.70
$\frac{S_{direct}}{S_{indirect}} = 10$ radius (mm)	3.55	7.48	20.3
$\frac{S_{direct}}{S_{indirect}} = 5$ radius (mm)	8.28	20.8	> 23

TABLE IV
SENSITIVITIES VALUES FROM RAT SIMPLIFIED BRAIN SHAPED ^{11}C SOURCES: LEFT AND RIGHT CAUDATE PUTAMEN (L. CPU. AND R. CPU.), LEFT AND RIGHT HARDERIAN GLANDS (L. HG. AND R. HG.), CEREBELLUM, AND REST OF BRAIN. THE SENSOR IS IMPLANTED INTO THE LEFT CAUDATE PUTAMEN REGION. THE SENSITIVITY IS THE NUMBER OF DETECTED EVENTS RELATIVE TO THE ACTIVITY CONCENTRATION IN THE SIMPLIFIED LEFT CAUDATE PUTAMEN REGION

Structure name	Direct sens. (cps · Bq^{-1} · mm^3) contribution to the total	Indirect sens. (cps · Bq^{-1} · mm^3) contribution to the total
R.o.B.	$(1.11 \pm 0.01) \times 10^{-1}$ 7.65%	$(2.27 \pm 0.05) \times 10^{-2}$ 26.05%
Cereb.	$< 1 \times 10^{-5}$	$(6.28 \pm 0.35) \times 10^{-4}$ 0.72%
L. CPu.	1.34 ± 0.01 92.35%	$(4.69 \pm 0.03) \times 10^{-2}$ 53.81%
R. CPu.	$(1.78 \pm 0.60) \times 10^{-5}$ 0.00%	$(3.73 \pm 0.09) \times 10^{-3}$ 4.28%
L. HG.	$< 1 \times 10^{-5}$	$(5.59 \pm 0.11) \times 10^{-3}$ 6.41%
R. HG.	$< 1 \times 10^{-5}$	$(7.61 \pm 0.12) \times 10^{-3}$ 8.73%

nonuniformity IU is equal to 7.53 %. The edge to center difference and the center region integral nonuniformity may have to be taken into account for experimental quantification of radiotracer concentrations using uniformity corrections.

C. Brain Phantom

Sensitivities in the brain phantom, with ^{11}C sources, are summarized in Table IV. As anticipated from the cylindrical phantom studies, the direct sensitivity is largely dominated by the activity in the implanted volume, L.CPu. [(1.34 $\pm$ 0.01) cps·Bq^{-1}·mm^3, 92.35 % of the total direct sensitivity], with a small contribution from the R.O.B. [(1.11 $\pm$ 0.01) $\times$ 10^{-1} cps·Bq^{-1}·mm^3, 7.65 % of the total direct sensitivity] and a marginal contribution from other regions.

The small contribution from the R.O.B. is partly attributable to the 0.9 mm height section of the pixels matrix inside this region. The signal measured only from pixels inside the L.CPu. leads to a direct sensitivity from L.CPu. of (1.29 $\pm$ 0.01)cps·Bq^{-1}·mm^3 but the direct sensitivity from the R.O.B. is reduced by a factor of 1.91 [(5.81 $\pm$ 0.03) $\times$ 10^{-2} cps·Bq^{-1}·mm^3].

Indirect sensitivity remains low, in particular for remote regions. The direct to indirect sensitivity ratio from the whole phantom is 16.7, but 53.8 % of the indirect sensitivity comes from the implanted volume.

This result confirms our confidence into the ability of the measured signal to reflect the local radioactivity concentration and not to be overtaken by indirect detection of remote hot spots like harderian glands.

D. Deposited Energy

Fig. 8(a) shows for each type of particle the deposited energy spectrum in the whole sensor, located at the center of the cylindrical ^{18}F source. When we split the sensitive volume into pixels (30$\times$50 μm^2 each) and we keep, for each event, the pixel with the highest deposited energy, the spectrum loses its high energy components [see Fig. 8(b)], because of the shorter distance limits and consequently shorter particles path in the pixel.

Positron and electron spectra shapes show similarities: peaks are at 6.9 and 7.9 keV, respectively. On the other hand, photons present relatively lower energy

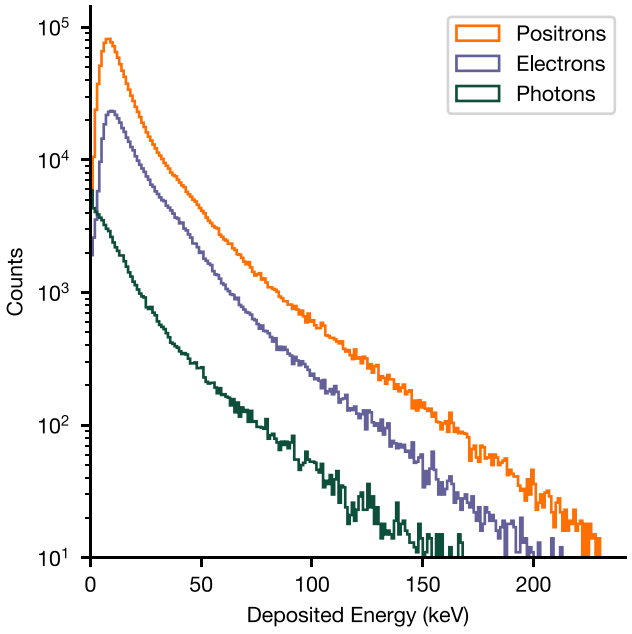

(a)

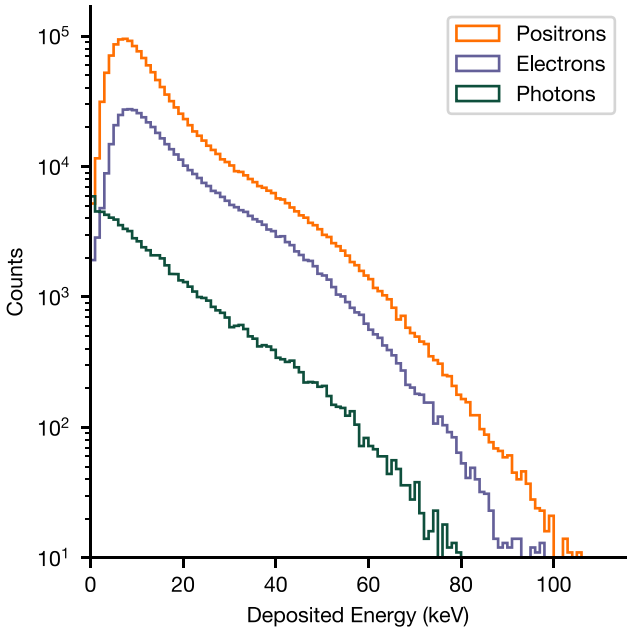

(b)

Fig. 8. Deposited energy spectra in an homogeneous ^{18}F solution, for each type of incident particle. (a) Deposited energy in the entire sensor. (b) Deposited energy spectrum in sensor pixels. In case of multiple pixels hit in the same event, the highest deposited energy in one pixel is kept.

depositions. The contributions below 4 keV represent 24.3 % of the photons spectrum whereas they account for only 7.15 % of the positrons spectrum. Table V summarizes the deposited energy distribution of direct positrons.

As explained in Section III-B, for the MAPS sensor model we expect an energy threshold smaller than a few keV to be enough to remove electronic noise. Hence, these spectra

TABLE V
PEAK, MEDIUM, AND MEAN DEPOSITED ENERGY IN THE PIXELS FOR DIRECT DETECTION ONLY, INTO A WATER ^{18}F SOURCE

Isotopes	^{18}F	^{11}C	^{15}O
E_{peak} (keV)	6.9	7.2	6.1
E_{median} (keV)	11.0	9.51	8.72
E_{mean} (keV)	15.1	12.9	11.4
fraction $<$ 1 keV	0.37 %	0.44 %	0.59 %
fraction $<$ 10 keV	44.3 %	52.9 %	59.0 %

confirm that at least one pixel is able to detect the incident particle in most of the cases: in an ^{18}F water solution, with 30 $\times$ 50 μm^2 pixels, the median energy is estimated to 11.0 keV. If we consider an hypothetical energy threshold value between 1 and 10 keV, we may lose between 0.37 % and 44.3 % of the signal. This strong effect of the threshold on the sensor sensitivity highlights the need for a low noise sensor, and hence the use of an energy threshold as low as possible. For other isotopes, similar results were found and are presented in Table V.

E. Effect of Sensitive Thickness

Increasing the sensor sensitive thickness leads to an increase of sensitivity for all particles as illustrated in Fig. 9. For ^{18}F, the direct sensitivity increases from (8.83 $\pm$0.01) $\times$ 10^{-1} cps·Bq^{-1}·mm^3 for a 18 μm sensitive thickness to (1.54 $\pm$ 0.01) cps·Bq^{-1}·mm^3 for the largest sensitive thickness (190 μm). Meanwhile, the indirect sensitivity also increases from (3.59 $\pm$ 0.01) $\times$ 10^{-1} cps·Bq^{-1}·mm^3 to (9.93 $\pm$ 0.01) $\times$ 10^{-1} cps·Bq^{-1}·mm^3.

However, the lower increase of sensitivities to incident electrons and positrons relatively to photons leads to a decrease of the direct to indirect positron sensitivity ratio as the thickness of the probe increases: from (2.46 $\pm$ 0.01) at 18 μm to (1.55 $\pm$ 0.01) at 190 μm. Consequently a tradeoff between the direct sensitivity and direct to indirect sensitivity ratio has to be made. A thin sensitive layer optimizes the direct to indirect sensitivity ratio (by up to a factor of 1.59) while a larger sensitive layer optimizes direct sensitivity (by up to a factor of 1.74).

Hence, when an energy threshold was applied we observed changes in this behavior, the ratio of direct to indirect sensitivity decreases for very low energy thresholds only. As shown in Fig. 10, the maximum direct to indirect sensitivity ratio achieved for a 18 μm probe thickness cannot be reached if the energy threshold is equal or superior to 5 keV. The optimal thickness associated with the maximum direct to indirect sensitivity ratio for a given energy threshold is presented in Fig. 11.

As the energy threshold increases, the sensitive thickness giving the optimum direct to indirect ratio increases too. A larger sensitive thickness always provide a better direct sensitivity, this demonstrates the interest of thick sensitive thickness in CMOS sensor if a high energy threshold is needed.

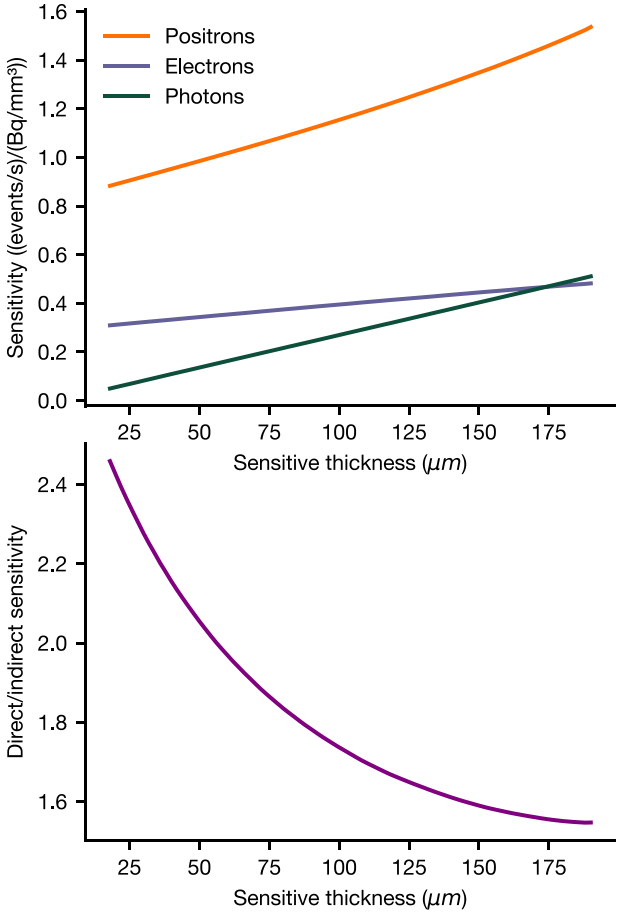

Fig. 9. Evolution of sensitivity and direct to indirect sensitivity ratio with sensitive thickness into a ^{18}F source. Sensitive thickness ranges between 18 μm, epitaxial layer thickness of our first prototype model and 190 μm, the full sensor thickness (excluding the 10 μm electronic layer).

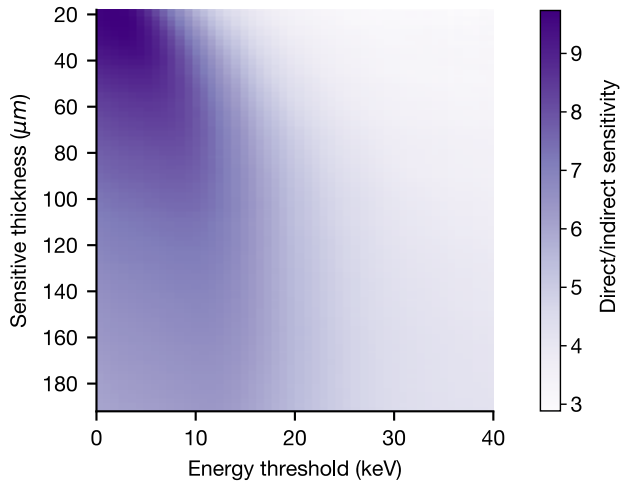

Fig. 10. Direct to indirect sensitivity ratio as a function of energy threshold and sensitive thickness for a ^{18}F source in water.

F. Pixels Size

Without energy threshold, the sensitivities are independent of the pixels dimension. As a matter of fact, smaller pixels lead to smaller energy depositions since only the pixel with the highest deposited energy is recorded.

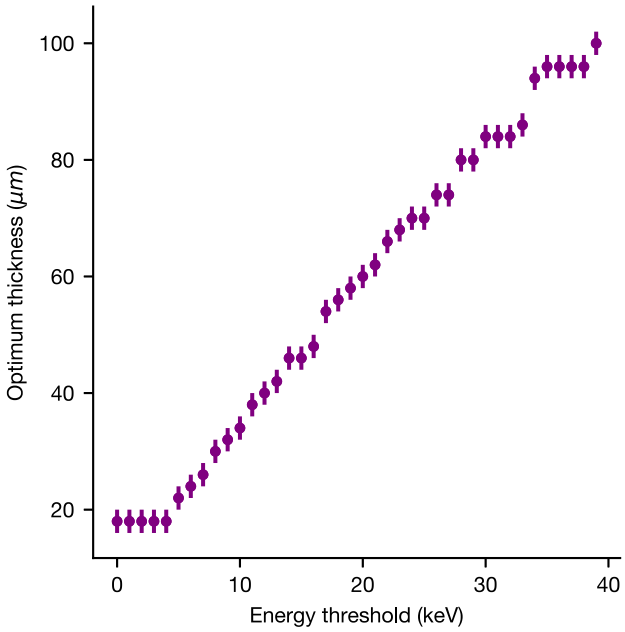

Fig. 11. Optimal thickness in terms of direct to indirect sensitivity ratio as a function of the energy threshold for an homogeneous ^{18}F source in water. The ratios were computed with a 2 μm step size for the thickness.

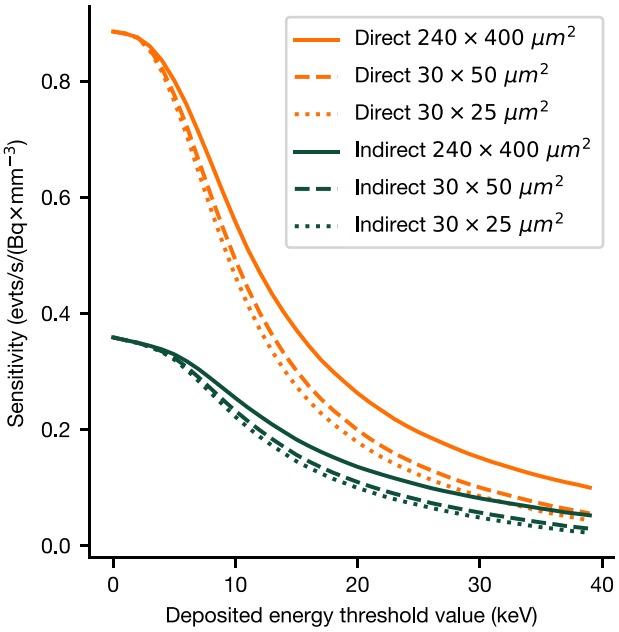

Fig. 12. Evolution of sensitivity of a ^{18}F source in water with deposited energy threshold for three different pixel sizes. Sensitive thickness is 18 μm, pixel sizes are 240 × 400 μm^2, 30 × 50 μm^2, and 30 × 25 μm^2, the total sensitive area remains constant (480 × 6400 μm^2).

However, when the energy threshold increases, smaller pixels with smaller energy depositions are more affected and some particles passing through the sensitive volume are not detected.

Fig. 12 presents the variations of the direct and indirect sensitivities as a function of energy threshold for three layouts of pixels arrays with the same total sensor area (480×6400 μm^2) : 16×128 pixels of 30×50 μm^2, as foreseen for our first prototype, 16×256 smaller pixels of 30×25 μm^2 and 2×16 larger pixels of 240×400 μm^2, comparable to the size of the PIXSIC pixels (200 × 500 μm^2).

With a 10 keV energy threshold, the effect of the pixel size on the direct sensitivity remains low, (5.19 ± 0.01) $\times$ 10^{-1} cps·Bq^{-1}·mm^3 for the smaller pixels versus (6.08 ± 0.01) $\times$ 10^{-1} cps·Bq^{-1}·mm^3 for the larger pixels, (2.42 ± 0.01) $\times$ 10^{-1} cps·Bq^{-1}·mm^3 and (2.71 ± 0.01) $\times$ 10^{-1} cps·Bq^{-1}·mm^3 for the indirect sensitivity of the smaller and larger pixels, respectively.

The ratio between direct and indirect sensitivity decreases with the energy threshold and is always slightly better for larger pixels. At a 10 keV energy threshold, this ratio is 2.14 ± 0.01 for the smaller pixels and 2.24 ± 0.01 for the larger pixels.

IV. Discussion

We aim to develop a probe suited for the detection of positrons in rodent brain tissues. The instrumental requirements for such a device are of diverse nature and every step is critical : sensitivity, quantification, image quality, biocompatibility, invasiveness, and mechanical robustness. In this paper we have presented some expected detection performances in terms of isoefficiency volume, sensitivity, and deposited energy. We also have explored how some design parameters impact performances.

This Monte Carlo study sets the MAPSSIC performances above the previous β^+ sensitive implants, notably it predicts a better sensitivity than the PIXSIC sensor. The 22.5 % larger equivalent sensitivity is explained first by the amplification at the level of the pixel, which allows to set a minimal energy threshold, whereas the sensitivity of the PIXSIC sensor required a 20 keV threshold. It also benefits from the larger sensitive region of the MAPSSIC probe (480 μm instead of 200 μm), thanks to a strong reduction of the nonsensitive area (guard rings) on the sensor edges (the full sensor width, including guard rings, was 690 μm for the PIXSIC sensor, instead of 610 μm on this MAPSSIC model). Thanks to the thin 18 μm thick sensitive area, we have also demonstrated a substantial improvement of the direct to indirect sensitivity ratio: 1.58 times larger compared to a similar sensor with a full sensitive thickness. Since the PIXSIC probe has been validated within a pharmacological context, we interpret this result as an evidence of the MAPSSIC sensor ability in terms of sensitivity. Compared to scintillating fibers probes [7], we will get an autonomous device, together with the benefits of a higher 2-D number of pixels and less signal from remote sources.

Besides their potential imaging capabilities, the current design of the pixels allows us to tackle issues related to brain radioactivity uptake heterogeneities with regard to the large field of view of the probe. As shown in the simplified brain phantom, when the sensor field of view extends over the volume of interest, the signal suffers from a contribution attributable to tracer concentration in nearby regions where the tracer also binds. However, as the probe position in the brain is known, the pixelated nature of the probes allows us to distinguish the events between their source region.

Since the pixel size does not influence detection performances with low energy thresholds, small pixels can be designed to allow for better spatial resolution. Although other effects related to the pixel sizes must also be investigated. For example, energy consumption and heat emission must be reduced as much as possible in order to increase the system autonomy and limit its invasiveness.

Unlike tomographs systems such as microPET or the wearable RatCAP, MAPSSIC and other intracerebral microprobes will not be able to provide full brain images. However, they appear as a complementary tools to study brain local dynamic processes, in particular for behavior neuroimaging or when the anesthesia is a limit.

The simulated sensor shows radiotracers sensitivity comparable to microPET. For the ^{11}C-raclopride model the direct sensitivity from the L.CPu. was evaluated at 1.34 cps·Bq^{-1}·mm^3 in a 67.375 mm^3 volume, thus, a 1.99 % mean direct efficiency in the L.CPu. For comparison, the rodent microPET devices presented in [24] perform a peak detection efficiency between 2.06 % (microPET R4) and 6.72 % (Inveon) (with a 350-650 keV energy window). For the Inveon microPET, the maximum true count rate in a cylindrical rat-sized phantom (60 mm diameter, 96 mm long), was measured to 1020 kcps at an activity of 118 MBq (350–650 keV energy window), thus a mean efficiency of 0.86 % in this phantom [25]. The RatCAP wearable tomograph performs a point source efficiency of 0.7 % (with an energy threshold of 150 keV) and a peak true counts rate of about 30 kcps at 350 kBq·cm^{-3} in a 19 cm^3 phantom filling the field of view, thus a mean efficiency in the phantom of 0.45 % [26]. These results confirm that MAPSSIC will benefit of the methodological tools of the microPET for dynamic studies: similar radiotracer doses and comparable time-activity curves.

This paper will drive the next sensor design. The Monte Carlo results have already allowed us to refine our β^+ sensor model. The direct to indirect sensitivity, considered as a signal to noise ratio, will be maximized by a thin sensitive layer. It has driven the first design to use the thinnest epitaxial layer. Nonetheless, the sensitivity also benefits from a deep epitaxial layer, consequently we expect fully depleted CMOS to provide us a substantial improvement.

Sensitivity is depicted as the strongest limit for the use of β^+ probes in biological experiments [27]. It defines how we handle the signal temporal and spatial dynamics and imposes a constraint on the probe surface, hence on its invasiveness. Consequently, we consider the probe sensitivity, i.e., its epitaxial thickness, as a parameter to maximize, even to the expense of a slightly lower direct to indirect sensitivity ratio.

Furthermore, the usual parallel between signal to noise ratio and direct to indirect sensitivity could be discussed since the solid angle effect restrains the indirect sensitivity from remote sources. As an example, the simplified brain phantom results showed that 53.8 % of the indirect signal originates from the implanted region. Moreover, this ratio allows to better understand and optimize the measurements by taking into account the pixels location inside the brain. In the simplified brain model, the ratio of the signal originating from the L. CPu. to the signal originating from outside of it is 9.18, but if we occult the pixels inside the R.O.B region (where 14 % of the sensitive region is implanted), it increases up to of 14.6.

The probe thickness and width, and therefore its invasiveness, is constrained by the sensitivity requirements but also by mechanical and technical constraints. To ensure the robustness of the sensor the thickness was thin down to 200 μm. The width of 610 μm was chosen close to PIXSIC dimensions. PIXSIC probe, with a 200×690 μm^2 section, produced consistent results compared to microPET in pharmacological studies without uptake modification attributable to tissue damages [28]. Consequently, we are confident that the implantation will not be a major limitation for the measurements.

Moreover, microdialysis cylindrical intracerebral probes with 340 μm outer diameter have shown to not significantly influence ^{11}C-raclopride experiments [29], although inducing a widespread and prolonged decrease in glucose metabolism [30], [31]. More important, Schiffer *et al.* [31] highlighted that the major issue to interpret the effects of probes implantation is the number of experimental variables that limits the relevance of comparison between experiments. As an example, in contrast to Schiffer *et al.* works, Glorie *et al.* [27] demonstrated the disruptive effect of their 750 μm outer diameter probes on striatal receptors binding and tracer delivery to the implanted region, but it is difficult to distinguish the impact of the larger diameter from other experimental conditions. In one case the measures were done immediately after the 750 μm probe implantation while in the second case the cannulae implantation was performed two days before imaging. As a matter of fact, Benveniste *et al.* [30] have shown that the time between surgery and measurement can influence microdialysis results and suggest a 24 h recovery time.

β^- sources have been widely used for the study of charged particle sensors using CMOS technology, in particular 2.2 MeV β^- from ^{90}Sr sources. Nonetheless, specific applications of β^+ or β^- detectors remain limited. As of today we have identified only two other CMOS applications of β^+ and β^- sensing [32], [33]. We interpret our results as a confirmation of the relevance of MAPS technology for direct β^+ sensing. As a consequence the first sensor prototype has been manufactured based on this Monte Carlo study and design.

With this first MAPS-based prototype, Monte Carlo simulations will be compared against experimental results in order to evaluate the accuracy of the Monte Carlo model. It will allow studying the effect of several parameters which were not included in our model as charges drift in silicon, exact energy threshold, or signal post-processing. Experimental measurements will also assess the sensor counting linearity over activity concentration variations, dark counts rate, and sensitivity to visible light.

Beyond electronic and physical testing of the sensor, the future probe developments will focus of the integration of the sensor into a robust and autonomous system. The probe also shall be adapted to be used with stereotaxic surgical tools and we plan to ensure biocompatibility by covering the sensor with a layer parylene C polymer as previously done for PIXSIC [9]. The first *in vivo* testings will aim to validate the surgical implantation procedure, the biocompatibility, and the detection performances on anesthetized animals. Once validated, experiments on awake then on freely moving animals will be performed.

The *in vivo* measurements and quantification procedure should follow the well validated one developed for PIXSIC described in [11] and [28]. In particular two probes are usually inserted, one in the region of interest and one in a reference tissue (for example the cerebellum for ^{18}F-MPPF or ^{11}C-raclopride studies). In these studies, the specific binding is defined as the difference between the activity in the region of interest and the activity in a reference tissue, accounting for nonspecific binding and free radiotracer activity.

As discussed in [8], the quantification for surface or distant beta sensors is limited by the difficulty to correctly evaluate the distance to the source as well as the attenuation in the non-radioactive medium between them. For intracerebral probes, if we neglect source heterogeneities in the volume of high efficiency, we benefit from Monte-Carlo and experimental sensitivity values obtained with a simpler source geometry. These sensitivity values are easier to use for quantification without correction. Furthermore, the experimental validation of this Monte Carlo model will allow us to use it for more precise predictions within a realistic brain phantom and source distribution. This will allow us to investigate the effects of sources heterogeneities on activity concentration quantification and our ability to extract spatial information.

REFERENCES

[1] S. R. Cherry, "Functional whole-brain imaging in behaving rodents," *Nat. Methods*, vol. 8, no. 4, pp. 301–303, 2011.

[2] A. R. Aarons, A. Talan, and W. K. Schiffer, "Experimental protocols for behavioral imaging: Seeing animal models of drug abuse in a new light," in *Brain Imaging in Behavioral Neuroscience* (Current Topics in Behavioral Neurosciences), vol. 11, C. Carter and J. Dalley, Eds. Heidelberg, Germany: Springer, 2012.

[3] A. K. O. Alstrup and D. F. Smith, "Anaesthesia for positron emission tomography scanning of animal brains," *Lab. Animals*, vol. 47, no. 1, pp. 12–18, 2013.

[4] V. D. Patel, D. E. Lee, D. L. Alexoff, S. L. Dewey, and W. K. Schiffer, "Imaging dopamine release with positron emission tomography (PET) and ^{11}C-raclopride in freely moving animals," *Neuroimage*, vol. 41, no. 3, pp. 1051–1066, 2008.

[5] A. Z. Kyme, V. W. Zhou, S. R. Meikle, and R. R. Fulton, "Real-time 3D motion tracking for small animal brain PET," *Phys. Med. Biol.*, vol. 53, no. 10, pp. 2651–2666, 2008.

[6] D. Schulz *et al.*, "Simultaneous assessment of rodent behavior and neurochemistry using a miniature positron emission tomograph," *Nat. Methods*, vol. 8, no. 4, pp. 347–352, 2011.

[7] L. Zimmer *et al.*, "Sic, an intracerebral β^+-range–sensitive probe for radiopharmacology investigations in small laboratory animals: Binding studies with ^{11}C-raclopride," *J. Nucl. Med.*, vol. 43, no. 2, pp. 227–233, 2002.

[8] M. T. Wyss *et al.*, "A beta-scintillator for surface measurements of radiotracer kinetics in the intact rodent cortex," *NeuroImage*, vol. 48, no. 2, pp. 339–347, 2009.

[9] J. Godart *et al.*, "PIXSIC: A pixellated beta-microprobe for kinetic measurements of radiotracers on awake and freely moving small animals," *IEEE Trans. Nucl. Sci.*, vol. 57, no. 3, pp. 998–1007, Jun. 2010.

[10] J. Märk *et al.*, "A wireless beta-microprobe based on pixelated silicon for *in vivo* brain studies in freely moving rats," *Phys. Med. Biol.*, vol. 58, no. 13, pp. 4483–4500, 2013.

[11] L. Balasse *et al.*, "PIXSIC: A wireless intracerebral radiosensitive probe in freely moving rats," *Mol. Imag.*, vol. 14, no. 9, pp. 484–489, 2015.

[12] T. Hirono *et al.*, "CMOS pixel sensors on high resistive substrate for high-rate, high-radiation environments," *Nucl. Instrum. Methods Phys. Res. A Accelerators Spectr. Detectors Assoc. Equ.*, vol. 831, pp. 94–98, Sep. 2016.

[13] G. Aglieri, "The ALPIDE pixel sensor chip for the upgrade of the ALICE inner tracking system," *Nucl. Instrum. Methods Phys. Res. A Accelerators Spectr. Detectors Assoc. Equ.*, vol. 845, pp. 583–587, Feb. 2017.

[14] A. Lauria *et al.*, "Experimental study for an intraoperative probe for ^{18}F imaging with a silicon pixel detector," *Nucl. Instrum. Methods Phys. Res. A Accelerators Spectr. Detectors Assoc. Equ.*, vol. 576, no. 1, pp. 198–203, 2007.

[15] S. Senyukov *et al.*, "Charged particle detection performances of CMOS pixel sensors produced in a process with a high resistivity epitaxial layer," *Nucl. Instrum. Methods Phys. Res. A Accelerators Spectr. Detectors Assoc. Equ.*, vol. 730, pp. 115–118, Dec. 2013.

[16] S. Jan *et al.*, "Gate: A simulation toolkit for PET and SPECT," *Phys. Med. Biol.*, vol. 49, no. 19, pp. 4543–4561, 2004.

[17] S. Jan *et al.*, "GATE V6: A major enhancement of the gate simulation platform enabling modelling of CT and radiotherapy," *Phys. Med. Biol.*, vol. 56, no. 4, pp. 881–901, 2011.

[18] G. Paxinos, C. R. R. Watson, and P. C. Emson, "AChE-stained horizontal sections of the rat brain in stereotaxic coordinates," *J. Neurosci. Methods*, vol. 3, no. 2, pp. 129–149, 1980.

[19] M.-P. Garcia *et al.*, "OSSI-PET: Open-access database of simulated ^{11}C-raclopride scans for the Inveon preclinical PET scanner: Application to the optimization of reconstruction methods for dynamic studies," *IEEE Trans. Med. Imag.*, vol. 35, no. 7, pp. 1696–1706, Jul. 2016.

[20] *Performance Measurements of Gamma Cameras (NEMA NU 1-2012)*, Nat. Elect. Manuf. Assoc., Arlington, VA, USA, 2012.

[21] Y. Luo *et al.*, "Dynamic study of the hippocampal volume by structural MRI in a rat model of depression," *Neurol. Sci.*, vol. 35, no. 11, pp. 1777–1783, 2014.

[22] J. E. Wong, J. Cao, D. M. Dorris, and J. Meitzen, "Genetic sex and the volumes of the caudate-putamen, nucleus accumbens core and shell: Original data and a review," *Brain Struct. Function*, vol. 221, no. 8, pp. 4257–4267, 2016.

[23] J. Cal-González *et al.*, "Positron range effects in high resolution 3D PET imaging," in *Proc. IEEE Nucl. Sci. Symp. Conf. Rec. (NSS/MIC)*, 2009, pp. 2788–2791.

[24] A. L. Goertzen *et al.*, "NEMA NU 4-2008 comparison of preclinical PET imaging systems," *J. Nucl. Med.*, vol. 53, no. 8, pp. 1300–1309, 2012.

[25] B. J. Kemp, C. B. Hruska, A. R. McFarland, M. W. Lenox, and V. J. Lowe, "NEMA NU 2-2007 performance measurements of the Siemens Inveon^{TM} preclinical small animal PET system," *Phys. Med. Biol.*, vol. 54, no. 8, p. 2359, 2009.

[26] P. Vaska *et al.*, "Initial performance of the RatCAP, a PET camera for conscious rat brain imaging," in *Proc. IEEE Nucl. Sci. Symp. Conf. Rec.*, vol. 5, 2005, pp. 3040–3044.

[27] D. Glorie *et al.*, "MicroPET outperforms beta-microprobes in determining neuroreceptor availability under pharmacological restriction for cold mass occupancy," *Front. Neurosci.*, vol. 11, p. 47, Feb. 2017.

[28] L. Balasse *et al.*, "PIXSIC, a pixelated β^+-sensitive probe for radiopharmacological investigations in rat brain: Binding studies with [^{18}F] MPPF," *Mol. Imag. Biol.*, vol. 17, no. 2, pp. 163–167, 2015.

[29] W. K. Schiffer, D. L. Alexoff, C. Shea, J. Logan, and S. L. Dewey, "Development of a simultaneous PET/microdialysis method to identify the optimal dose of ^{11}C-raclopride for small animal imaging," *J. Neurosci. Methods*, vol. 144, no. 1, pp. 25–34, 2005.

[30] H. Benveniste, J. Drejer, A. Schousboe, and N. H. Diemer, "Regional cerebral glucose phosphorylation and blood flow after insertion of a microdialysis fiber through the dorsal hippocampus in the rat," *J. Neurochem.*, vol. 49, no. 3, pp. 729–734, 1987.

[31] W. K. Schiffer *et al.*, "Serial microPET measures of the metabolic reaction to a microdialysis probe implant," *J. Neurosci. Methods*, vol. 155, no. 2, pp. 272–284, 2006.

[32] W. Dulinski *et al.*, "Beta detection and imaging probe based on optimized CMOS monolithic active pixel sensors for open surgical and endoscopic cancer resection applications," in *Proc. IEEE Nucl. Sci. Symp. Conf. Rec. Nucl. Sci. Symp.*, 2010.

[33] J. Cabello *et al.*, "Digital autoradiography using room temperature CCD and CMOS imaging technology," *Phys. Med. Biol.*, vol. 52, no. 16, p. 4993, 2007.